

ACCEPTED MANUSCRIPT

## Microfabrication of polydimethylsiloxane–parylene hybrid microelectrode array integrated into a multi-organ-on-a-chip

To cite this article before publication: Dongxiao Zhang *et al* 2022 *Jpn. J. Appl. Phys.* in press <https://doi.org/10.35848/1347-4065/aca265>

### Manuscript version: Accepted Manuscript

Accepted Manuscript is “the version of the article accepted for publication including all changes made as a result of the peer review process, and which may also include the addition to the article by IOP Publishing of a header, an article ID, a cover sheet and/or an ‘Accepted Manuscript’ watermark, but excluding any other editing, typesetting or other changes made by IOP Publishing and/or its licensors”

This Accepted Manuscript is © 2022 The Japan Society of Applied Physics.

During the embargo period (the 12 month period from the publication of the Version of Record of this article), the Accepted Manuscript is fully protected by copyright and cannot be reused or reposted elsewhere.

As the Version of Record of this article is going to be / has been published on a subscription basis, this Accepted Manuscript is available for reuse under a CC BY-NC-ND 3.0 licence after the 12 month embargo period.

After the embargo period, everyone is permitted to use copy and redistribute this article for non-commercial purposes only, provided that they adhere to all the terms of the licence <https://creativecommons.org/licenses/by-nc-nd/3.0>

Although reasonable endeavours have been taken to obtain all necessary permissions from third parties to include their copyrighted content within this article, their full citation and copyright line may not be present in this Accepted Manuscript version. Before using any content from this article, please refer to the Version of Record on IOPscience once published for full citation and copyright details, as permissions will likely be required. All third party content is fully copyright protected, unless specifically stated otherwise in the figure caption in the Version of Record.

View the [article online](#) for updates and enhancements.

## Microfabrication of polydimethylsiloxane–parylene hybrid microelectrode array integrated into a multi-organ-on-a-chip

Dongxiao Zhang<sup>1</sup>, Jiandong Yang<sup>1</sup>, Yoshikazu Hirai<sup>1, 2\*</sup>, Ken-ichiro Kamei<sup>3</sup>, Osamu Tabata<sup>1, 4</sup>, and Toshiyuki Tsuchiya<sup>1</sup>

1. *Department of Micro Engineering, Kyoto University, Kyoto daigaku-katsura, Nishikyo-ku, Kyoto 615-8540, Japan*
2. *Department of Mechanical Engineering and Science, Kyoto University, Kyoto daigaku-katsura, Nishikyo-ku, Kyoto 615-8540, Japan*
3. *Institute for Integrated Cell-Material Sciences, Kyoto University, Yoshida-Ushinomiya-cho, Sakyo-ku, Kyoto 606-8501, Japan*
4. *Department of Mechanical and Electrical System Engineering, Kyoto University of Advanced Science, Gotanda-cho, Yamanouchi, Ukyo-ku, Kyoto 615-8577, Japan*

*Corresponding Author: Yoshikazu HIRAI, Email: hirai@me.kyoto-u.ac.jp*

### Abstract

Multi-organ-on-a-chip have attracted extensive attention because they hold great potential for advancing drug discovery and development by recapitulating human physiological conditions. However, they often lack on-chip analytical technologies for the *in situ* non-invasive real-time monitoring of organ tissue responses to pharmaceutical compounds over extended durations. Here, we introduce the microfabrication of a multi-organ-on-a-chip by integrating two indispensable components into a polydimethylsiloxane (PDMS)-based microfluidic device: a pneumatic-actuated micropump to generate a circulation flow for organ-organ interaction and a parylene-insulated microelectrode array (MEA) for electrophysiological analysis. We demonstrated that the pumping performance of the micropump was sufficient for recapitulating the metabolite interaction, and the measured impedance magnitude was comparable to that of state-of-the-art MEA devices. The experimental results suggest that the present microfabrication has potential such as for measurement of electrophysiological parameters under recapitulating metabolite interaction, enabling a more comprehensive drug testing *in vitro*.

## 1. Introduction

Microfluidic-based *in vitro* cell-culture models are termed “microphysiological systems (MPSs)” and are designed to mimic physiologically relevant functions of human organs and tissues [1-3]. Unlike conventional cell-culture models currently used in drug discovery and development, microfluidic-based cell-culture models can be more predictive of *in vivo* biology owing to the dynamic environment control in the microfluidic device for cell growth, differentiation, migration, and maturation. Therefore, these devices are expected to replace animal models, which are often inaccurate in predicting human physiology because of species differences, leading to reduced costs and time in pharmaceutical research and development [4, 5]. Among on-chip platforms, compartmentalized multiorgan platforms with the circulatory system integrated into a single device, known as multi-organ-on-a-chip [6-9], hold great potential for advancing drug development, disease modeling, and precision medicine, because they can mimic the blood flow in the human body with closed-loop culture media by means of a micropump. Such medium circulation recapitulates organ-organ interactions and helps emulate the dynamic exposure of organ cells to drugs and drug metabolites, offering valuable insights into systemic toxicity [10-14]. However, we continue to rely on post facto methods for data collection, including histology, fluorescence imaging after sample cell fixation, and biomolecular assays [15-17]. Therefore, a crucial aspect in the device design is the integration of a measurement system that allows quantitative and non-invasive functional analysis of cultured cells in real-time.

Currently, cardiotoxicity is a major cause of drug candidate failure in clinical tests and is responsible for the retraction of numerous drugs from the market [18-20]. For cardiotoxicity assessment *in vitro*, the employed device would require an electrical readout system for the electrophysiological parameters of cardiomyocytes corresponding to the changes in the electrocardiogram parameters such as the ventricular depolarization/repolarization (QT) interval and spontaneous beating frequency. Several detection methods are available to obtain key electrophysiological parameters [21], such as patch clamp electrodes [22], light-addressable potentiometric sensors (LAPSs) [23], and field-effect transistors (FETs) [24]. Among the various methods, microelectrode array (MEA)-embedded culture dishes [25, 26] have been widely used as a non-invasive, electrical readout system to measure cardiomyocyte extracellular field potentials (FPs) at the cell population level. Additionally, the change in the

1  
2  
3  
4  
5  
6  
7 FP duration (FPD) measured with the MEA is directly related to the QT interval in the human  
8 heart's electrical cycle [27, 28]. Thus, this method has been combined with single-organ chip  
9 devices and has been used to analyze cardiomyocyte responses to pharmaceutical compounds  
10 *in situ* over long durations [29-34]. However, although most of the reported MEA-integrated  
11 devices [30, 31, 33, 34] can help test cardiotoxicity, interactions with other organs cannot be  
12 tested. Moreover, to assess multiple organ interactions while reducing bubble formation and  
13 non-selective absorption of hydrophobic small molecules (e.g., metabolites and drug candidates)  
14 due to the additional tubing required for fluidic couplings, pneumatically or electrically actuated  
15 on-chip micropumps [35, 36] are required to reflect physiologically relevant interactions.  
16 Notably, none of the multi-organ-on-a-chip devices that allow the assessment of  
17 electrophysiological parameters have been coupled to microfluidic platforms with on-chip  
18 micropumps. Therefore, a novel microfabrication strategy that can help integrate MEA and  
19 micropump components into the same microfluidic device while maintaining the ease of device  
20 fabrication and process reliability of the functional components is desired in this field.  
21  
22  
23  
24  
25  
26  
27  
28  
29

30  
31 Herein, we present the microfabrication of a multi-organ-on-a-chip with an MEA, by  
32 assuming the measurement of electrophysiological activities of cardiac tissues induced by  
33 heart-liver interactions. This device is fabricated mainly using PDMS through soft lithography,  
34 with a three-layer structure comprising a perfusion layer, an MEA layer, and a control layer, as  
35 illustrated in Fig. 1. The present microfabrication allows seamless integration of two  
36 indispensable components: a pneumatic-actuated micropump for accurate and reliable flow  
37 control and an MEA for the real-time monitoring of cells. To improve the metal adhesion  
38 between gold and PDMS and the process reliability of MEA integration into the PDMS-based  
39 microfluidic device, we employed an insulating and biocompatible material, parylene-C. On  
40 the parylene-PDMS hybrid MEA layer, a flexible-thin membrane for micropump actuation and  
41 parylene-insulated MEA components for the cell chamber are simultaneously realized.  
42 Therefore, this paper focuses on the seamless integration method of MEA in the PDMS-based  
43 device by considering each material properties related to the multilayer soft lithography process  
44 and the technical characterizations of micropump and MEA with analytical simulations. We  
45 demonstrated the efficiency of the micropump fabrication with simulation-aided grayscale  
46 lithography for accurate operation of the micropump through flow rate measurements and finite  
47 element method (FEM) simulation, and the electrical characteristics of a parylene-insulated  
48 electrode were assessed by electrical impedance measurements.  
49  
50  
51  
52  
53  
54  
55  
56  
57  
58  
59  
60

## 2. Multi-organ-on-a-chip with microelectrode array device

### 2.1 Device configuration

Figures 1a and b show illustrations of the multi-organ-on-a-chip with MEA device, wherein a structure with three layers is bonded to a glass substrate from top to bottom: a perfusion layer, an MEA layer, and a control layer. To achieve closed-loop culture-medium circulation in a single device, a pneumatic-actuated micropump and microvalves are directly embedded with soft-lithography process because pneumatic actuation method realizes large membrane deformation with an easily controllable hydraulic pressure and small footprint than the other methods, e.g., electromagnetic, and piezoelectric micropump [36]. The micropump located between two cell-culture chambers comprises three adjacent microvalves of square membrane with sequential actuation to provide periodic peristaltic motion. The flow within the device is controlled by selectively opening and closing normally open microvalves in the “push-up” configuration (Fig. 1b). In addition, a cross-section geometry of channel in the perfusion layer is analytically designed in rounded shape to be sealed completely by the deformed membrane. The microvalves enable individual accessibility for each cell culture chamber and a sophisticated control of the cell and culture medium for the test. The following are some of the requirements for the materials used in the device: 1) Biocompatibility, 2) Gas permeability, 3) Light transparency, 4) High moisture resistance to prevent electrode corrosion, and 5) Low stiffness to realize pneumatic-actuated pumping. Among several polymeric materials [37, 38], PDMS meets the above requirements as the structural material of the device [39, 40].

For mapping the cardiac electrophysiology, the Au electrodes in the MEA layer are arranged in the form of a 3×6 array and designed with a pitch of 260  $\mu\text{m}$  along the length of one cell chamber to avoid the crosstalk of the electrical signals between the electrodes (Fig. 2). The electrical interconnects extend from the electrodes to the contact pads patterned on the surface of the MEA layer. The contact pads are defined to be 250  $\mu\text{m}$  × 250  $\mu\text{m}$  (length and width). The electrode traces are insulated by parylene-C, which has good material characteristics such as biocompatibility, low dielectric constant, and high resistivity [41-43]. Parylene-C also shows low water and gas permeability, light transparency, chemical inertness, nontoxicity, and nonbiodegradability. Moreover, it can prevent the poor adhesion and cracks in the Au film owing to the different degrees of thermal expansion between the metal and the PDMS [44, 45],

1  
2  
3  
4  
5  
6  
7 thus enabling a more repeatable and reliable fabrication of MEA patterns on the PDMS surface.  
8 Although parylene-C offers these advantages, it has a higher stiffness than PDMS [41, 46-48].  
9 Use of substrates with low stiffness induces a more similar cardiac phenotype to that shown *in*  
10 *vivo* [49-52]. The parylene film deposited on PDMS affects the stiffness of the MEA layer,  
11 because of which the PDMS will no longer have the advantage of minimizing inhibition against  
12 cardiomyocyte response and realizing pneumatic-actuated pumping. Therefore, the parylene-C  
13 insulating layer for the MEA was thinned through an etching process and completely removed  
14 from the micropump locations for lower pressurization to deform the PDMS membrane. This  
15 PDMS–parylene hybrid MEA layer combining the advantages of both the materials shows a  
16 good balance between the stiffness of PDMS and the insulation of parylene while maintaining  
17 a metal adhesion between the PDMS layers.  
18  
19  
20  
21  
22  
23  
24  
25

26 Figure 1c shows a photomask design of three-layer structure and realistic top view of the  
27 device. The perfusion layer contains three sets of two compartmentalized cell-culture chambers  
28 (length: 4650  $\mu\text{m}$ ; width: 2150  $\mu\text{m}$ ; height: 220  $\mu\text{m}$ ) and the sample inlet/outlet holes indicated  
29 in blue, in which cardiomyocytes and hepatocytes are cultured. This cell-culture chamber size  
30 is designed to supply the required growth factors, the drugs, and allowing for reduced shear  
31 stress [14]. Microchannels (width: 200  $\mu\text{m}$ ; height: 45  $\mu\text{m}$ ) called “flow channels” were  
32 designed for easy introducing of the cells from the inlet holes and used to interconnect the two  
33 cell-culture chambers. The control layer contains dead-end microchannels (width: 15  $\mu\text{m}$ ;  
34 height: 45  $\mu\text{m}$ ) called “control channels” and the pressure inlet holes indicated in green, which  
35 are routed to cross the flow channels, forming a thin, flexible PDMS membrane for micropump  
36 and microvalves (200  $\mu\text{m} \times 200 \mu\text{m}$ ; thickness: 20  $\mu\text{m}$ ) at their intersection by the MEA layer  
37 and supplying hydraulic pressure to the membrane. Thus, to form the 200 $\times$ 200  $\mu\text{m}^2$  square  
38 PDMS membrane, the narrow control channels at the location of the micropump and  
39 microvalves were designed to be 200  $\mu\text{m}$  wide (length: 1.6 mm). The location of the micropump  
40 and valves and the routing of the control channels were carefully designed so that the operation  
41 of the micropump does not interfere with the electrical measurement with the MEA.  
42  
43  
44  
45  
46  
47  
48  
49  
50  
51  
52  
53  
54

## 55 2.2 Design of flow channel for micropump

56 For an effective micropump operation, the flow channels at microvalve locations have a  
57 rounded cross-sectional profile because at least one of the microvalves should always seal the  
58  
59  
60

channel completely to generate a net flow rate in a specific direction without leakage [53-56]. The microvalve with a square membrane can generate a larger deformation compared to a circular membrane. Thus, the micropump structure with square membranes and rounded cross-sectional channel can completely block the fluid flow and provide accurate and reliable control over the fluid flow in the perfusion layer with small footprint.

To achieve the design optimization of micropump through analytical simulation, a square PDMS membrane deformation was first analyzed using finite element analysis (FEA) with COMSOL Multiphysics (v.5.2, COMSOL). Here, a Young's modulus ( $E$ ) of 1.9 MPa and a Poisson's ratio ( $\nu$ ) of 0.499 were employed, under a PDMS curing process condition at 80 °C [48]. This primary simulation was implemented in a simplified square PDMS membrane structure using the Neo-Hookean hyperelastic material model, which, although a simple approach to model hyper-elastic materials, is sufficiently accurate in the case of small strains [46]. The initial bulk modulus ( $\kappa$ ), Lamé parameter ( $\mu$ ), and density of the material ( $\rho$ ) were set to  $5.0 \times 10^8$  Pa,  $1.0 \times 10^5$  N/m<sup>2</sup>, and 970 kg/m<sup>3</sup>, respectively. Figure 3a shows the simulated result on a  $200 \times 200$   $\mu\text{m}^2$  square PDMS membrane having a thickness of 20  $\mu\text{m}$  for a 45  $\mu\text{m}$  high flow channel. This PDMS membrane profile at a pressure of 65 kPa was transformed into the target flow channel profile of the photoresist mold, that is precisely fabricated by grayscale lithography with numerical process optimization. In this configuration, the ideal volume of swept liquid in one cycle of peristaltic micropump consisting of three chambers is 1.23 nL. Here, the total liquid volume of the present device, including the flow channels and two cell-culture chambers, was approximately 260 nL. At a driving frequency of 1 Hz, circulatory can be achieved in about 210 seconds, which is sufficient for recapitulating the metabolite interaction between two organs in the device [14]. Furthermore, to discuss relationship between the applied pressure and measured flow volume, a contact analysis of the membrane deformation in the flow channel was performed as shown in Figures 3b and c.

### 2.3 Design of microelectrode array

The MEA requires a low impedance to achieve a high signal-to-noise ratio (SNR). The recording electrodes are typically characterized and discussed by their impedance at 1 kHz. Based on the previously reported measurements [57], the target impedance was set to 90 k $\Omega$  at 1 kHz. Below this impedance value, the electrical signal of the cardiomyocyte could be detected. A suitable electrode diameter for cardiomyocytes can be numerically analyzed with the cell-

1  
2  
3  
4  
5  
6  
7 electrode model [58-60] by considering the electrical double layer formed at the electrode–  
8 electrolyte interface. The corresponding capacitance of the electric double layer can be  
9 described by the Gouy–Chapman–Stern model as a series capacitance of the Helmholtz double-  
10 layer capacitance and the Gouy–Chapman diffuse layer capacitance [61]. The values for these  
11 numerical simulations can be found elsewhere [62, 63]. Based on the numerical simulation  
12 results and the size of the cardiomyocytes, the diameter of the MEA electrodes was finally  
13 designed, ranging from 80 to 100  $\mu\text{m}$ .  
14  
15  
16  
17  
18  
19

### 20 21 **3. Fabrication**

22 The microfabrication technique employed for the device (Fig. 1d) is the typical multilayer  
23 soft lithography that combines soft lithography with the capability to bond multiple patterned  
24 layers of PDMS [64, 65]. Figure 4a shows the schematic of the detailed fabrication procedure  
25 for the entire device. In this process, a uniform PDMS mortar (uncured PDMS) was achieved  
26 using a thin-film PDMS microcontact printing method [66, 67] and was used for bonding each  
27 layer. Prior to the bonding process, the perfusion layer was cut partially to accommodate the  
28 contact pads of MEA as shown in Fig. 1a. The entire device bonded to the glass substrate was  
29 finally cured in a convection oven at 80  $^{\circ}\text{C}$  for 12 h.  
30  
31  
32  
33  
34  
35  
36  
37

#### 38 **3.1 Perfusion and control layers**

39 The perfusion layer comprises cell culture chambers and flow channels of different heights.  
40 The mold fabrication for the perfusion layer followed the multilayer lithography principle,  
41 which combines standard and grayscale lithography (for cell culture chambers and  
42 microchannels, respectively). First, a dry-film type of negative photoresist (45 $\mu\text{m}$ ; TMMF  
43 S2045, Tokyo Ohka Kogyo) was laminated 4 times on the surface of a 4-inch Si wafer with a  
44 thickness of 180  $\mu\text{m}$ . UV exposure was carried out on a mask aligner (MUM-0001 [68], Japan  
45 Science Engineering) using a Cr-patterned glass mask for the thick mold of cell culture  
46 chambers. Then, a post-exposure bake (PEB) at 90  $^{\circ}\text{C}$  for 5 min was performed after the UV  
47 exposure process. The sample was developed in a propylene glycol monomethyl ether acetate  
48 (PGMEA) solution at a temperature of 23  $^{\circ}\text{C}$ . Next, a positive photoresist (PMER P-LA900PM,  
49 Tokyo Ohka Kogyo) for grayscale lithography was spin-coated twice with a final thickness of  
50 45  $\mu\text{m}$  on the Si wafer. A pre-bake process was performed at 115  $^{\circ}\text{C}$  for 12 min in a convection  
51  
52  
53  
54  
55  
56  
57  
58  
59  
60



oven. A relaxation time (20 min at a temperature of 23 °C and a humidity of 40%) for photoresist rehydration was provided between pre-bake and the UV exposure process. Subsequently, digital micromirror device (DMD)-based grayscale lithography (DL-1000GS/KCH, NanoSystem Solutions) was used to fabricate the target flow channel profile, shown in Fig. 3a, which was analyzed by the FEM simulation. The development temperature was 21 °C, which is controlled carefully to not affect the dissolution rate of photoresist.

Digital grayscale lithography is an effective method to obtain arbitrary three-dimensional (3D) photoresist profiles by modulating the intensity of ultraviolet (UV) light according to the grayscale mask data. However, the fabrication of the target profile using 3D lithography is not straightforward because of the complex photoresist interaction with UV light and the development process [69-72]. To compensate for the two nonlinear effects and generate optimal process parameters, we adopted a numerical simulation approach that can automatically determine the best combination of the four process parameters summarized in Table I: 1) Exposure dose, 2) 256-level digital grayscale mask, 3) Focal position of the DMD-based lithographic projection apparatus, and 4) Development time, which has been previously described [71]. In contrast, the control layer was simply cast from a 30  $\mu\text{m}$ -thick negative photoresist mold (TMMR S2000, Tokyo Ohka Kogyo).

After mold fabrication, the PDMS base and curing agent (Sylgard 184 kit, Dow Corning) were thoroughly mixed at a ratio of 10:1 (w/w) and poured onto the molds. Here, peeling a thin MEA-control bonded layer from the Si substrate would cause mechanical stress to the multilayer, potentially resulting in cracks in Au electrodes, wrinkles, and damage on Parylene-PDMS interfaces. In order to avoid these negative effects and allow for cells observation under the invert microscope, PDMS thickness for the control layer was carefully controlled to  $2.5 \pm 0.5$  mm. Finally, the PDMS for the control and perfusion layers was cured in a convection oven at 80 °C for 20 min and 4 h, respectively.

### 3.2 Microelectrode array layer

To deposit the electrodes on the PDMS layer while avoiding the poor metal adhesion and cracks, we employed parylene-C, which can be conformally vapor deposited as an insulator and used as a substrate material for MEA fabrication. The PDMS-parylene hybrid MEA layer was fabricated using the following process (Fig. 4b). First, Si carrier wafer was dehydrated at 150 °C

1  
2  
3  
4  
5  
6  
7 then deposited 5  $\mu\text{m}$ -thick parylene-C using a parylene deposition system (Labcoater PDS 2010,  
8 KISCO). Next, a Hexamethyldisilazane (HMDS; OAP, Tokyo Ohka Kogyo) and positive  
9 photoresist (2  $\mu\text{m}$ ; OFPR-800 54cp, Tokyo Ohka Kogyo) was spin coated, and patterned at the  
10 electrode sites and contact pads by standard lithography. The parylene layer for the electrode  
11 sites was then etched 3  $\mu\text{m}$  thick using  $\text{O}_2$  plasma (Power 100 W: Pressure 40 Pa: Flow rate 40  
12 sccm; FA-1, SAMCO). A 200 nm-thick Au film was deposited on the surface using electron  
13 beam deposition (EB-1200, Canon Anelva) and patterned through a photoresist mask,  
14 comprising the electrodes, associated traces, and contact pads. The Au film of the MEA pattern  
15 was created by wet-etching (Aurum, Kanto Kagaku) at 27  $^\circ\text{C}$ . Subsequently, the MEA pattern  
16 was covered by another parylene-C layer with a thickness of 2  $\mu\text{m}$ . The Au film sandwiched  
17 between the parylene-C layers was spin-coated in a final 20  $\mu\text{m}$ -thick PDMS membrane for the  
18 pneumatic-actuated micropump. After bonding to the control layer by curing in a convection  
19 oven at 80  $^\circ\text{C}$  for 4 h, the MEA-control bonded structure was mechanically peeled off from the  
20 carrier wafer. Finally, the parylene-C layer on the backside was removed about 2  $\mu\text{m}$  thick by  
21  $\text{O}_2$  plasma etching (Power 100 W: Pressure 40 Pa: Flow rate 40 sccm) to open at the location  
22 of the electrode sites and contact pads to allow direct contact.  
23  
24  
25  
26  
27  
28  
29  
30  
31  
32  
33

34 Additionally, in the present fabrication of the MEA layer, parylene-C on the entire area  
35 except for MEA insulation was mechanically removed using a tweezer after  $\text{O}_2$  plasma etching  
36 of the parylene in the small gap formed by the bulk-PDMS mask (Fig. 4c). Parylene removal  
37 of the MEA layer and increased PDMS area is useful for maintaining the flexibility of the  
38 PDMS membrane as much as possible to actuate the pneumatic-actuated micropump. This  
39 fabrication sequence can prevent functionalization of the PDMS surface due to  $\text{O}_2$  plasma  
40 treatment and sticking of the deformed PDMS membrane to the flow channel during the  
41 micropump operation. Moreover, the surface area of PDMS on the MEA layer facing the  
42 perfusion layer is increased by the etching of parylene-C, resulting the strong bond and  
43 fabrication of leakage-free devices. Therefore, the PDMS-parylene hybrid MEA layer  
44 combining the advantages of both materials shows a good balance between structural stiffness  
45 and MEA insulation while maintaining a simple microfabrication process.  
46  
47  
48  
49  
50  
51  
52  
53  
54  
55  
56  
57  
58  
59  
60

## 4. Experimental setup

### 4.1 Micropump control

The pneumatic micropump was actuated by applying a positive hydraulic pressure from the control layer. The control channel was first filled with distilled water to prevent gas permeation across the PDMS membrane and the consequent formation of bubbles in the liquid-filled flow channels. Subsequently, metal pins and Teflon tubes were used to connect the inlet of the control channels and the pneumatic system to a compressed nitrogen gas source (regulated in the 0–200 kPa pressure range). The pressure actuation and release of the microvalves were controlled and operated using a real-time controller (cRIO-9022, National Instruments) via electromagnetic valves controlled using a custom-made LabVIEW software (Ver. 2019, National Instruments) in terms of the frequency and sequence of the ON/OFF control. In this study, a six-stage actuation pattern was employed to control the ON/OFF operation of the solenoid valves as shown in Fig. 5 [65]. The flow rates were regulated by the actuation frequency for the sequential opening and closing of a set of three microvalves acting as a micropump.

### 4.2 Flow rate measurement

To evaluate the flow rates, micro-beads (20  $\mu\text{m}$  in diameter; Polysciences) were used to visualize the culture medium flow and measure the flow distance. Prior to the measurements, the microfluidic channel was coated with 1% (w/v) bovine serum albumin (BSA, Sigma-Aldrich) in PBS for 2 h at 25  $^{\circ}\text{C}$  to prevent non-specific adhesion on the flow channels and cell culture chambers. Micro-beads were suspended in 1% (w/v) BSA solution at  $1 \times 10^6$  beads/mL. Subsequently, a bead-containing solution was introduced into the device. After the flow stabilized using the micropump, the movement of the micro-beads was captured using a CMOS camera (EO-4010, Edmund Optics) at a frame rate of 60 fps. A self-written MATLAB (Ver. R2019b, MathWorks) program was used to detect the positions of individual micro-beads in each image, which are linked over the image sequence and resulted in individual trajectories. From the trajectories recorded in the center line of the flow channel, the individual flow rates of the micro-beads were determined by averaging the pulsatile characteristics of the flow generated by the peristaltic working principle.

The average flow velocity  $\bar{u}$  was half the micro-bead velocity at the centerline ( $U_{max}$ ), as defined by the Navier–Stokes equation:

$$\bar{u} = \frac{1}{2} U_{max} \quad (1)$$

The volumetric flow rates were calculated by multiplying the flow velocity with the cross-sectional area of the microfluidic channel.

### 4.3 Impedance measurement

The MEA was characterized by electrical impedance spectroscopy (EIS) in a three-electrode measurement setup. The impedance and phase measurements were carried out using an impedance/gain-phase analyzer (Frequency Response analyzer 1260, Solartron) by applying an AC amplitude of 50 mV in the frequency range of 10 Hz–100 kHz. The measurements were performed in the presence of a phosphate buffer saline (PBS) solution (D-PBS, Fujifilm Wako).

## 5. Results and discussion

### 5.1 Micropump characterization

The driving pressure and actuation frequency of cyclic operation in Fig. 5 are two key factors affecting the performance of the micropump. First, the effect of the driving pressure on the volumetric (pumping) flow rate was investigated at a frequency of 1.5 Hz, as shown in Fig. 5a. Each dot represents the mean  $\pm$  standard deviation (SD) ( $n = 3$ ). The pumping flow rate was constant at 0 nL/min until reaching a pressure of 50 kPa, at which the PDMS membrane contacted the flow channel, and then increased gradually with pressure, exhibiting a maximum at a pressure of approximately 150 kPa owing to the full sealing of the flow channel. At pressures  $>150$  kPa, the flow rate stabilized at 36.0 nL/min. The validity of this pressure dependence of the flow rate was confirmed by the FEA results, considering a contact analysis of the PDMS membrane deformation in the flow channel, as shown in Figs. 3b and c. The pressure of 50 kPa in the experiment agrees well with the pressure of 57 kPa in the analysis where the deformed PDMS starts to seal the flow channel. In addition, the pump chamber was fully sealed at pressures  $>140$  kPa in the analysis, resulting in a constant membrane stroke volume in the pump chamber (the difference between the maximum and minimum chamber volumes as the membrane actuates once) and therefore a constant flow rate in the measurements. Because the photoresist profile measured using a mechanical stylus profiler (Dektak XT-S,

1  
2  
3  
4  
5  
6  
7  
8  
9  
10  
11  
12  
13  
14  
15  
16  
17  
18  
19  
20  
21  
22  
23  
24  
25  
26  
27  
28  
29  
30  
31  
32  
33  
34  
35  
36  
37  
38  
39  
40  
41  
42  
43  
44  
45  
46  
47  
48  
49  
50  
51  
52  
53  
54  
55  
56  
57  
58  
59  
60

Brüker) agreed well with the target profile (Fig. 6) and parylene-C on the MEA layer was completely removed, the error between the measurements and FEA results, albeit small, may have resulted from the material properties of the PDMS. For example, the Young's modulus of PDMS can vary from 50 kPa to 4 MPa depending on the process conditions [48, 73]. The flow rate became less stable when the pressure was increased above 200 kPa. Therefore, a pressure of 150 kPa was selected because achieving a constant and reliable pumping is an important feature of a micropump particularly when integrated in multi-organ-on-a-chip devices.

Next, the frequency response under a pressure of 150 kPa was investigated, as shown in Fig. 5b. Each dot represents mean  $\pm$  SD ( $n = 3$ ). The flow rate shows a consistent trend with the driving frequency and almost linearly increases with the frequency until it reaches a peak value of 63.0 nL/min at a frequency of 2.9 Hz. Based on our previous experiments [14], this pumping performance is sufficient for recapitulating the metabolite interaction between cardiomyocytes and hepatocytes in the present device. The flow rate then decreases with further increase in the frequency because the membrane deformation could not synchronize with the pneumatic actuation at higher frequencies, resulting in a decreased membrane stroke volume in the pump chamber. Additionally, the flow rate and frequency exhibit a nonlinear relationship because of the complex nonlinear interaction between the PDMS membrane deformation, driving pressure, and hydrostatic pressure present in the micropump [74-76]. These results demonstrate that the present micropump fabrication with the combination of simulation-aided grayscale lithography and removal of parylene-C on the MEA layer can ensure a complete sealing of the flow channel at the designed pressure, enabling accurate and reliable micropump operation in the device. In addition, the flow rate in this micropump can increase linearly in a certain frequency range and can be adjusted easily and accurately using the magnitude of the pressure and frequency.

## 5.2 Electrochemical characterization

To characterize the MEA, the influence of the electrode size on the surface impedance was first investigated under static conditions (i.e., without the medium flow in the device). Figure 7 compares the impedance magnitude and phase measured under different diameters of the MEA electrodes (80, 90, and 100  $\mu\text{m}$ ). Generally, the spectrum of an Au electrode–PBS solution is dominated by the impedance of the electrode–electrolyte interface; the low-frequency part of the curves is mostly related to the electrode impedance contribution, whereas the high-frequency part is related to the electrolyte impedance. In the measurements, the decrease in the

1  
2  
3  
4  
5  
6  
7 impedance magnitude with increasing frequency and the reversal of the phase angle from  
8 almost  $-90^\circ$  toward  $0^\circ$  suggest a capacitive behavior. By comparing the impedance magnitude  
9 at 1 kHz, which is the typical frequency used for signal recording, electrodes having a larger  
10 diameter were found to have a lower impedance value, as summarized in Table II. These values  
11 were obtained by averaging the impedance spectra of eight randomly selected electrodes. For  
12 example, the impedance value (mean  $\pm$  SD) at 1 kHz was  $36.9 \pm 5.5$  k $\Omega$  for electrodes with  
13 a diameter of 90  $\mu\text{m}$ , which falls in the anticipated range for metal electrodes with an exposed  
14 surface dimension of 6362  $\mu\text{m}^2$  in area and satisfies the requirement for cardiomyocyte FP  
15 detection, i.e., below 90 k $\Omega$  at 1 kHz. The variation in the impedance magnitude from electrode  
16 to electrode on the same MEA layer is crucial in assessing the detection of similar signals. The  
17 measurements indicate a small variation from electrode to electrode on the same MEA layer  
18 and thus validate the good quality of the present microfabrication. The measured impedance  
19 values of the Au electrodes at 1 kHz are comparable to the impedance values of state-of-the-art  
20 MEA devices [26, 77].  
21  
22  
23  
24  
25  
26  
27  
28  
29  
30

31 Generally, additional process such as Pt black or poly(3,4-ethylenedioxythiophene) doped  
32 with poly(styrene sulfonate) (PEDOT:PSS) are employed to fabricate electrodes with low  
33 impedance [26]. The low impedance values obtained at 1 kHz without any additional process  
34 can be attributed to the relatively large surface roughness of the Au film deposited on parylene-  
35 C and exposed to O<sub>2</sub> plasma because the increased effective surface area leads to lower the  
36 electrode impedance. Atomic force microscopy (AFM) in the tapping mode (MultiMode 8,  
37 Bruker) was carried out to measure the surface morphology of the electrode surface. The surface  
38 roughness ( $R_a$ ) in the probed sample area of  $1 \times 1$   $\mu\text{m}^2$  was 15.4 nm, which is higher than that of  
39 the same 200 nm-thick Au film deposited on a glass [78]. In addition to the impedance  
40 measurements under the temporal static condition, measurements under sequential medium  
41 perfusion are anticipated. The impedance changes in the MEA due to the maximum flow rate  
42 of 63.0 nL/min were also measured with a diameter of 90  $\mu\text{m}$ . The measured impedance was  
43 lower than that under the static condition, though the difference was less than 1%. The  
44 impedance could be further optimized by tuning the thickness and deposition rate of parylene-  
45 C and Au films.  
46  
47  
48  
49  
50  
51  
52  
53  
54  
55  
56

57 Next, the Au electrode–PBS electrolyte interface was characterized using an electrical  
58 equivalent circuit model. As mentioned previously, when a metal electrode is immersed in an  
59  
60

electrolyte, an electrode–electrolyte double-layer capacitance is formed on its surface. The equivalent circuit for the Au electrode–PBS electrolyte, called the Randles circuit model [79–81], can be modeled using a constant phase element (CPE), replacing the electric double-layer capacity in parallel with the charge transfer resistance  $R_{tr}$ , which are then connected in series with the solution resistance  $R_s$ . The mathematical expression of the CPE electrode element impedance is [82]:

$$Z_{CPE} = \frac{1}{K(j\omega)^n} \quad (2)$$

where  $K$  is the frequency-independent, phenomenological parameter,  $\omega$  is the angular frequency, and  $n$  is the fractional exponent indicating the deviation in the CPE from ideal capacitive behavior. When  $n = 1$ , it behaves as an ideal capacitor, whereas when  $n = 0$ , it behaves as an ideal resistor. The parameter  $K$  has a complex unit of  $F \cdot s^{n-1}$ , where  $F$  is Farads, and  $s$  is seconds. Applying this Randles circuit model and fitting the impedance plots, shown in Fig. 7a, with the MATLAB software, we can obtain approximate numerical values for the individual electrical components. The fitted values of  $R_s$ ,  $R_{tr}$ , and  $K$  for electrodes with a diameter of 90  $\mu\text{m}$  (area:  $6.36 \times 10^3 \mu\text{m}^2$ ) were 2.14  $\text{k}\Omega$ , 29.6  $\text{M}\Omega$ , and 99.2  $\mu\text{F} \cdot \text{s}^{n-1}/\text{cm}^2$ , respectively. The conductivity of PBS is estimated to be 2.59 S/m, which is close to that of typical PBS. In addition,  $n$  is determined to be 0.94, which is close to 1 for an ideal capacitor, and the value of  $K$  is similar to that reported for Au electrodes [83]. These experimental results demonstrated that the electrode sites in the MEA were completely opened by the final  $\text{O}_2$  plasma etching and worked as well as typical Au electrodes.

## 6. Conclusions

We presented the design, fabrication method, and preliminary characterization of a multi-organ-on-a-chip with MEA. This device was fabricated mainly using PDMS through soft lithography, where a three-layer structure was bonded to a glass substrate, considering the material properties related to the process. For accurate and reliable micropump operation in the device, we combined DMD-based grayscale lithography optimized by numerical optimization methods for soft lithography. The parylene–PDMS hybrid MEA layer enabled the monolithic integration of the pneumatic micropump and MEA in the multi-organ-on-a-chip. The measurement results of the pumping flow rate in the device showed that drugs and metabolites can move from one chamber to another within 2.5 min, which is sufficient for recapitulating

1  
2  
3  
4  
5  
6  
7  
8  
9  
10  
11  
12  
13  
14  
15  
16  
17  
18  
19  
20  
21  
22  
23  
24  
25  
26  
27  
28  
29  
30  
31  
32  
33  
34  
35  
36  
37  
38  
39  
40  
41  
42  
43  
44  
45  
46  
47  
48  
49  
50  
51  
52  
53  
54  
55  
56  
57  
58  
59  
60

metabolite interactions between cardiomyocytes and hepatocytes in the. In addition, the impedance measured at 1 kHz was  $36.9 \pm 5.5 \text{ k}\Omega$  for electrodes with a diameter of 90  $\mu\text{m}$ ; this value is comparable to those of state-of-the-art MEA devices.

The present device comprising a multi-layer PDMS structure is not optimal, as the applicability is limited due to the absorption of hydrophobic small molecules by the PDMS [84-86]. Such absorption causes a discrepancy between the nominally administrated concentration and actual cellular exposures. These absorption problems can be prevented by lipophilic coatings [87] or compensated using experimental measurements combined with simulation models [88, 89]. Further efforts to realize the full potential of mechanically actuable devices, novel materials that are both flexible and optically transparent, while being minimally absorptive for small molecules, will need to be developed. Finally, the present device is expected to be substituted for conventional end-point assays and help fill the gap between *in vivo* and *in vitro* conditions, serving as an excellent platform for drug testing. With the incorporation of appropriate model tissues, both physiological and pathological conditions can be studied thoroughly for better clinical treatments.

## Acknowledgments

This work was supported in part by JSPS KAKENHI Grant Number JP19H02572, JP 18KK0306, the Toyota Physical and Chemical Research Institute, and the Ebara Hatakeyama Memorial Foundation. Part of the present research was conducted at the Kyoto University Nano Technology Hub as part of the “Nanotechnology Platform Project” sponsored by the Ministry of Education, Culture, Sports, Science and Technology, Japan (MEXT). The authors gratefully acknowledge the help extended by T. Omaki, I. Yamauchi, and Dr. N. Yamashita (Kyoto University).



## References

- [1] S.N. Bhatia, D.E. Ingber, Microfluidic organs-on-chips, *Nat Biotechnol*, 32(2014) 760-772.
- [2] B. Zhang, M. Radisic, Organ-on-a-chip devices advance to market, *Lab Chip*, 17(2017) 2395-2420.
- [3] S.M. Park, S. Eom, H. Hong, J. Yoon, S.J. Lee, B.C. Kim, H.W. Kim, D.S. Kim, Reconstruction of in vivo-like in vitro model: Enabling technologies of microfluidic systems for dynamic biochemical/mechanical stimuli, *Microelectron Eng*, 203(2019) 6-24.
- [4] E.W. Esch, A. Bahinski, D. Huh, Organs-on-chips at the frontiers of drug discovery, *Nat Rev Drug Discov*, 14(2015) 248-260.
- [5] J.M. Ayuso, K.Y. Park, M. Virumbrales-Munoz, D.J. Beebe, Toward improved in vitro models of human cancer, *APL Bioeng*, 5(2021) 010902.
- [6] S.H. Lee, J.H. Sung, Organ-on-a-Chip technology for reproducing multiorgan physiology, *Adv Healthc Mater*, 7(2018) 1700419.
- [7] Y.I. Wang, C. Carmona, J.J. Hickman, M.L. Shuler, Multiorgan microphysiological systems for drug development: Strategies, advances, and challenges, *Adv Healthc Mater*, 7(2018) 1701000.
- [8] J.H. Sung, Y.I. Wang, N. Narasimhan Sriram, M. Jackson, C. Long, J.J. Hickman, M.L. Shuler, Recent advances in Body-on-a-Chip systems, *Anal Chem*, 91(2019) 330-351.
- [9] Q. Ramadan, M. Zourob, Organ-on-a-chip engineering: Toward bridging the gap between lab and industry, *Biomicrofluidics*, 14(2020) 041501.
- [10] J.P. Wikswo, E.L. Curtis, Z.E. Eagleton, B.C. Evans, A. Kole, L.H. Hofmeister, W.J. Matloff, Scaling and systems biology for integrating multiple organs-on-a-chip, *Lab Chip*, 13(2013) 3496-3511.
- [11] K. Ronaldson-Bouchard, G. Vunjak-Novakovic, Organs-on-a-Chip: A fast track for engineered human tissues in drug development, *Cell Stem Cell*, 22(2018) 310-324.
- [12] A. van den Berg, C.L. Mummery, R. Passier, A.D. van der Meer, Personalised organs-on-chips: Functional testing for precision medicine, *Lab Chip*, 19(2019) 198-205.
- [13] S. Fowler, W.L.K. Chen, D.B. Duignan, A. Gupta, N. Hariparsad, J.R. Kenny, W.G. Lai, J. Liras, J.A. Phillips, J. Gan, Microphysiological systems for ADME-related

- 1  
2  
3  
4  
5  
6 applications: current status and recommendations for system development and  
7 characterization, *Lab Chip*, 20(2020) 446-467.
- 8  
9  
10 [14] K. Kamei, Y. Kato, Y. Hirai, S. Ito, J. Satoh, A. Oka, T. Tsuchiya, Y. Chen, O. Tabata,  
11 Integrated heart/cancer on a chip to reproduce the side effects of anti-cancer drugs in vitro,  
12 *RSC Adv*, 7(2017) 36777-36786.
- 13  
14 [15] A. Junaid, A. Mashaghi, T. Hankemeier, P. Vulto, An end-user perspective on Organ-on-  
15 a-Chip: Assays and usability aspects, *Curr Opin Biomed Eng*, 1(2017) 15-22.
- 16  
17 [16] J.R. Soucy, A.J. Bindas, A.N. Koppes, R.A. Koppes, Instrumented microphysiological  
18 systems for real-time measurement and manipulation of cellular electrochemical  
19 processes, *iScience*, 21(2019) 521-548.
- 20  
21 [17] A.T. Young, K.R. Rivera, P.D. Erb, M.A. Daniele, Monitoring of microphysiological  
22 systems: Integrating sensors and real-time data analysis toward autonomous decision-  
23 making, *ACS Sens*, 4(2019) 1454-1464.
- 24  
25 [18] R.R. Shah, Cardiac repolarisation and drug regulation: assessing cardiac safety 10 years  
26 after the CPMP guidance, *Drug Saf*, 30(2007) 1093-1110.
- 27  
28 [19] N. Ferri, P. Siegl, A. Corsini, J. Herrmann, A. Lerman, R. Benghozi, Drug attrition during  
29 pre-clinical and clinical development: Understanding and managing drug-induced  
30 cardiotoxicity, *Pharmacol Ther*, 138(2013) 470-484.
- 31  
32 [20] J. Kieninger, A. Weltin, H. Flamm, G.A. Urban, Microsensor systems for cell metabolism  
33 - from 2D culture to organ-on-chip, *Lab Chip*, 18(2018) 1274-1291.
- 34  
35 [21] X. Wei, L. Zhuang, H. Li, C. He, H. Wan, N. Hu, P. Wang, Advances in multidimensional  
36 cardiac biosensing technologies: From electrophysiology to mechanical motion and  
37 contractile force, *Small*, 16(2020) 2005828.
- 38  
39 [22] L. Yobas, Microsystems for cell-based electrophysiology, *J Micromech Microeng*,  
40 23(2013) 083002.
- 41  
42 [23] X. Duan, T.M. Fu, J. Liu, C.M. Lieber, Nanoelectronics-biology frontier: From  
43 nanoscopic probes for action potential recording in live cells to three-dimensional cyborg  
44 tissues, *Nano Today*, 8(2013) 351-373.
- 45  
46 [24] J. Wang, L.P. Du, S. Krause, C.S. Wu, P. Wang, Surface modification and construction of  
47 LAPS towards biosensing applications, *Sens Actuator B-Chem*, 265(2018) 161-173.
- 48  
49 [25] R. Kim, S. Joo, H. Jung, N. Hong, Y. Nam, Recent trends in microelectrode array  
50 technology for in vitro neural interface platform, *Biomed Eng Lett*, 4(2014) 129-141.
- 51  
52  
53  
54  
55  
56  
57  
58  
59  
60

- 1  
2  
3  
4  
5  
6  
7 [26] C.M. Didier, A. Kundu, D. DeRoo, S. Rajaraman, Development of in vitro 2D and 3D  
8 microelectrode arrays and their role in advancing biomedical research, *J Micromech*  
9 *Microeng*, 30(2020) 103001.
- 10  
11 [27] S.R. Braam, L. Tertoolen, A. van de Stolpe, T. Meyer, R. Passier, C.L. Mummery,  
12 Prediction of drug-induced cardiotoxicity using human embryonic stem cell-derived  
13 cardiomyocytes, *Stem Cell Res*, 4(2010) 107-116.
- 14  
15 [28] C. van Noord, M. Eijgelsheim, B.H. Stricker, Drug- and non-drug-associated QT interval  
16 prolongation, *Br J Clin Pharmacol*, 70(2010) 16-23.
- 17  
18 [29] M. Stancescu, P. Molnar, C.W. McAleer, W. McLamb, C.J. Long, C. Oleaga, J.M. Prot,  
19 J.J. Hickman, A phenotypic in vitro model for the main determinants of human whole  
20 heart function, *Biomaterials*, 60(2015) 20-30.
- 21  
22 [30] V.J. Kujala, F.S. Pasqualini, J.A. Goss, J.C. Nawroth, K.K. Parker, Laminar ventricular  
23 myocardium on a microelectrode array-based chip, *J Mat Chem B*, 4(2016) 3534-3543.
- 24  
25 [31] F. Qian, C. Huang, Y.D. Lin, A.N. Ivanovskaya, T.J. O'Hara, R.H. Booth, C. J. Creek,  
26 H.A. Enright, D.A. Soscia, A.M. Belle, R. Liao, F.C. Lightstone, K.S. Kulp, E.K. Wheeler,  
27 Simultaneous electrical recording of cardiac electrophysiology and contraction on chip,  
28 *Lab Chip*, 17(2017) 1732-1739.
- 29  
30 [32] T. Ryyänen, M. Pekkanen-Mattila, D. Shah, J. Kreutzer, P. Kallio, J. Leikkala, K. Aalto-  
31 Setälä, Microelectrode array for noninvasive analysis of cardiomyocytes at the single-cell  
32 level, *Jpn J Appl Phys*, 57(2018) 117001.
- 33  
34 [33] Y. Asahi, T. Hamada, A. Hattori, K. Matsuura, M. Odaka, F. Nomura, T. Kaneko, Y. Abe,  
35 K. Takasuna, A. Sanbuissho, K. Yasuda, On-chip spatiotemporal electrophysiological  
36 analysis of human stem cell derived cardiomyocytes enables quantitative assessment of  
37 proarrhythmia in drug development, *Sci Rep*, 8(2018) 14536.
- 38  
39 [34] A. Alassaf, G. Tansik, V. Mayo, L. Wubker, D. Carbonero, A. Agarwal, Engineering  
40 anisotropic cardiac monolayers on microelectrode arrays for non-invasive analyses of  
41 electrophysiological properties, *Analyst*, 145(2019) 139-149.
- 42  
43 [35] A.K. Au, H.Y. Lai, B.R. Utela, A. Folch, Microvalves and Micropumps for BioMEMS,  
44 *Micromachines*, 2(2011) 179-220.
- 45  
46 [36] F. Forouzandeh, A. Arevalo, A. Alfadhel, D.A. Borkholder, A review of peristaltic  
47 micropumps, *Sens Actuator A-Phys*, (2021) 112602.
- 48  
49 [37] B.J. Kim, E. Meng, Review of polymer MEMS micromachining, *J Micromech Microeng*,
- 50  
51  
52  
53  
54  
55  
56  
57  
58  
59  
60

- 26(2016) 013001.
- [38] C. Ding, X. Chen, Q. Kang, X. Yan, Biomedical application of functional materials in Organ-on-a-Chip, *Front Bioeng Biotechnol*, 8(2020) 823.
- [39] J.C. McDonald, G.M. Whitesides, Poly(dimethylsiloxane) as a material for fabricating microfluidic devices, *Accounts Chem Res*, 35(2002) 491-499.
- [40] G. Liang, G.S. Guvanasen, L. Xi, C. Tuthill, T.R. Nichols, S.P. DeWeerth, A PDMS-based integrated stretchable microelectrode array (isMEA) for neural and muscular surface interfacing, *IEEE Trans Biomed Circuits Syst*, 7(2013) 1-10.
- [41] B.J. Kim, E. Meng, Micromachining of Parylene C for bioMEMS, *Polym Adv Technol*, 27(2016) 564-576.
- [42] J. Ortigoza-Diaz, K. Scholten, C. Larson, A. Cobo, T. Hudson, J. Yoo, A. Baldwin, A. Weltman Hirschberg, E. Meng, Techniques and considerations in the microfabrication of Parylene C microelectromechanical systems, *Micromachines*, 9(2018) 422.
- [43] M. Golda-Cepa, K. Engvall, M. Hakkarainen, A. Kotarba, Recent progress on parylene C polymer for biomedical applications: A review, *Prog Org Coat*, 140(2020) 105493.
- [44] N. Bowden, S. Brittain, A.G. Evans, J.W. Hutchinson, G.M. Whitesides, Spontaneous formation of ordered structures in thin films of metals supported on an elastomeric polymer, *Nature*, 393(1998) 146-149.
- [45] A. Muller, M.C. Wapler, U. Wallrabe, A quick and accurate method to determine the Poisson's ratio and the coefficient of thermal expansion of PDMS, *Soft Matter*, 15(2019) 779-784.
- [46] T.K. Kim, J.K. Kim, O.C. Jeong, Measurement of nonlinear mechanical properties of PDMS elastomer, *Microelectron Eng*, 88(2011) 1982-1985.
- [47] L.C.S. Nunes, Mechanical characterization of hyperelastic polydimethylsiloxane by simple shear test, *Mater Sci Eng A*, 528(2011) 1799-1804.
- [48] I.D. Johnston, D.K. McCluskey, C.K.L. Tan, M.C. Tracey, Mechanical characterization of bulk Sylgard 184 for microfluidics and microengineering, *J Micromech Microeng*, 24(2014) 035017.
- [49] B. Bhana, R.K. Iyer, W.L. Chen, R. Zhao, K.L. Sider, M. Likhitpanichkul, C. A. Simmons, M. Radisic, Influence of substrate stiffness on the phenotype of heart cells, *Biotechnol Bioeng*, 105(2010) 1148-1160.
- [50] M. Tallawi, R. Rai, A.R. Boccaccini, K.E. Aifantis, Effect of substrate mechanics on

- 1  
2  
3  
4  
5  
6  
7 cardiomyocyte maturation and growth, *Tissue Engineering Part B: Reviews*, 21(2015)  
8 157-165.
- 9  
10 [51] S.D. Boothe, J.D. Myers, S. Pok, J. Sun, Y. Xi, R.M. Nieto, J. Cheng, J.G. Jacot, The  
11 effect of substrate stiffness on cardiomyocyte action potentials, *Cell Biochemistry and*  
12 *Biophysics*, 74(2016) 527-535.
- 13  
14 [52] I. Jorba, D. Mostert, L.H.L. Hermans, A. van der Pol, N.A. Kurniawan, C.V.C. Bouten,  
15 *In vitro* methods to model cardiac mechanobiology in health and disease, *Tissue*  
16 *Engineering Part C: Methods*, 27(2021) 139-151.
- 17  
18 [53] V. Studer, G. Hang, A. Pandolfi, M. Ortiz, W.F. Anderson, S.R. Quake, Scaling properties  
19 of a low-actuation pressure microfluidic valve, *J Appl Phys*, 95(2004) 393-398.
- 20  
21 [54] E.P. Kartalov, A. Scherer, S.R. Quake, C.R. Taylor, W.F. Anderson, Experimentally  
22 validated quantitative linear model for the device physics of elastomeric microfluidic  
23 valves, *J Appl Phys*, 101(2007) 64505.
- 24  
25 [55] Y.-S. Lee, N. Bhattacharjee, A. Folch, 3D-printed Quake-style microvalves and  
26 micropumps, *Lab Chip*, 18(2018) 1207-1214.
- 27  
28 [56] D.N. Freitas, A. Mongersun, H. Chau, I.E. Araci, Tunable soft lithography molds enable  
29 rapid-prototyping of multi-height channels for microfluidic large-scale integration, *J*  
30 *Micromech Microeng*, 29(2019) 035009.
- 31  
32 [57] S.K. Rastogi, J. Bliley, D.J. Shiowski, G. Raghavan, A.W. Feinberg, T. Cohen-Karni,  
33 Graphene microelectrode arrays for electrical and optical measurements of human stem  
34 cell-derived cardiomyocytes, *Cell Mol Bioeng*, 11(2018) 407-418.
- 35  
36 [58] W. Franks, I. Schenker, P. Schmutz, A. Hierlemann, Impedance characterization and  
37 modeling of electrodes for biomedical applications, *IEEE Trans Biomed Eng*, 52(2005)  
38 1295-1302.
- 39  
40 [59] N. Joye, A. Schmid, Y. Leblebici, Electrical modeling of the cell-electrode interface for  
41 recording neural activity from high-density microelectrode arrays, *Neurocomputing*,  
42 73(2009) 250-259.
- 43  
44 [60] L.D. Xiao, Q.J. Liu, Z.Y. Hu, W. Zhang, H. Yu, P. Wang, A multi-scale electrode array  
45 (MSEA) to study excitation-contraction coupling of cardiomyocytes for high-throughput  
46 bioassays, *Sens Actuator B-Chem*, 152(2011) 107-114.
- 47  
48 [61] A.J. Bard, L.R. Faulkner, *Electrochemical Methods: Fundamentals and Applications*, 2  
49 ed., New York: John Wiley and Sons; 2000.
- 50  
51  
52  
53  
54  
55  
56  
57  
58  
59  
60

- 1  
2  
3  
4  
5  
6  
7 [62] T. Kiss, Electrical properties of the cardiac muscle cell membrane and its role in the  
8 excitation-contraction coupling, *Acta Biocchim Biophys Acad Scient Hung*, 12(1977)  
9 291-302.
- 10  
11 [63] K. Asakura, S. Hayashi, A. Ojima, T. Taniguchi, N. Miyamoto, C. Nakamori, C.  
12 Nagasawa, T. Kitamura, T. Osada, Y. Honda, C. Kasai, H. Ando, Y. Kanda, Y. Sekino, K.  
13 Sawada, Improvement of acquisition and analysis methods in multi-electrode array  
14 experiments with iPS cell-derived cardiomyocytes, *J Pharmacol Toxicol Methods*,  
15 75(2015) 17-26.
- 16  
17 [64] M.A. Unger, H.P. Chou, T. Thorsen, A. Scherer, S.R. Quake, Monolithic microfabricated  
18 valves and pumps by multilayer soft lithography, *Science*, 288(2000) 113-116.
- 19  
20 [65] T. Thorsen, S.J. Maerkl, S.R. Quake, Microfluidic large-scale integration, *Science*,  
21 298(2002) 580-584.
- 22  
23 [66] S. Satyanarayana, R.N. Karnik, A. Majumdar, Stamp-and-stick room-temperature  
24 bonding technique for microdevices, *J Microelectromech Syst*, 14(2005) 392-399.
- 25  
26 [67] M.A. Eddings, M.A. Johnson, B.K. Gale, Determining the optimal PDMS-PDMS  
27 bonding technique for microfluidic devices, *J Micromech Microeng*, 18(2008) 067001.
- 28  
29 [68] Y. Hirai, Y. Inamoto, K. Sugano, T. Tsuchiya, O. Tabata, Moving mask UV lithography  
30 for three-dimensional structuring, *J Micromech Microeng*, 17(2007) 199-206.
- 31  
32 [69] Y. Hirai, K. Sugano, T. Tsuchiya, O. Tabata, A three-dimensional microstructuring  
33 technique exploiting the positive photoresist property, *J Micromech Microeng*, 20(2010)  
34 065005.
- 35  
36 [70] J.G. Hur, Maskless fabrication of three-dimensional microstructures with high isotropic  
37 resolution: practical and theoretical considerations, *Appl Optics*, 50(2011) 2383-2390.
- 38  
39 [71] X. Ma, Y. Kato, F. van Kempen, Y. Hirai, T. Tsuchiya, F. van Keulen, O. Tabata,  
40 Experimental study of numerical optimization for 3-D microstructuring using DMD-  
41 based grayscale lithography, *J Microelectromech Syst*, 24(2015) 1856-1867.
- 42  
43 [72] Q. Deng, Y. Yang, H. Gao, Y. Zhou, Y. He, S. Hu, Fabrication of micro-optics elements  
44 with arbitrary surface profiles based on one-step maskless grayscale lithography,  
45 *Micromachines*, 8(2017) 314.
- 46  
47 [73] D. Fuard, T. Tzvetkova-Chevolleau, S. Decossas, P. Tracqui, P. Schiavone, Optimization  
48 of poly-di-methyl-siloxane (PDMS) substrates for studying cellular adhesion and motility,  
49 *Microelectron Eng*, 85(2008) 1289-1293.
- 50  
51  
52  
53  
54  
55  
56  
57  
58  
59  
60

- 1  
2  
3  
4  
5  
6  
7 [74] O.C. Jeong, S. Konishi, Fabrication and drive test of pneumatic PDMS micro pump, *Sens*  
8 *Actuator A-Phys*, 135(2007) 849-856.  
9
- 10 [75] J. Ni, F. Huang, B. Wang, B. Li, Q. Lin, A planar PDMS micropump using in-contact  
11 minimized-leakage check valves, *J Micromech Microeng*, 20(2010) 095033.  
12
- 13 [76] C.H. Chiou, T.Y. Yeh, J.L. Lin, Deformation analysis of a pneumatically-activated  
14 polydimethylsiloxane (PDMS) membrane and potential micro-pump applications,  
15 *Micromachines*, 6(2015) 216-229.  
16
- 17 [77] A. Susloparova, S. Halliez, S. Begard, M. Colin, L. Buee, S. Pecqueur, F. Alibart, V.  
18 Thomy, S. Arscott, E. Pallecchi, Y. Coffinier, Low impedance and highly transparent  
19 microelectrode arrays (MEA) for in vitro neuron electrical activity probing, *Sens Actuator*  
20 *B-Chem*, 327(2021) 128895.  
21
- 22 [78] A. Bonyar, P. Lehoczki, An AFM study regarding the effect of annealing on the  
23 microstructure of gold thin films, *in Proc. The 36th International Spring Seminar on*  
24 *Electronics Technology*, pp. 317-322. <https://doi.org/10.1109/ISSE.2013.6648265>.  
25
- 26 [79] I.R. Mineev, S.P. Lacour, Impedance spectroscopy on stretchable microelectrode arrays,  
27 *Appl Phys Lett*, 97(2010) 043707.  
28
- 29 [80] P.R. Rocha, P. Schlett, U. Kintzel, V. Mailander, L.K. Vandamme, G. Zeck, H.L. Gomes,  
30 F. Biscarini, D.M. de Leeuw, Electrochemical noise and impedance of Au  
31 electrode/electrolyte interfaces enabling extracellular detection of glioma cell populations,  
32 *Sci Rep*, 6(2016) 34843.  
33
- 34 [81] A. Wang, D. Jung, J. Park, G. Junek, H. Wang, Electrode-electrolyte interface impedance  
35 characterization of ultra-miniaturized microelectrode arrays over materials and  
36 geometries for sub-cellular and cellular sensing and stimulation, *IEEE Trans*  
37 *Nanobioscience*, 18(2019) 248-252.  
38
- 39 [82] J.B. Jorcin, M.E. Orazem, N. Pebere, B. Tribollet, CPE analysis by local electrochemical  
40 impedance spectroscopy, *Electrochim Acta*, 51(2006) 1473-1479.  
41
- 42 [83] A. Bonyar, G. Harsányi, CPE investigation of gold thin films, *in Proc. The 2011 IEEE*  
43 *17th International Symposium for Design and Technology in Electronic Packaging*  
44 *(SIITME)*, pp. 117-120. <https://doi.org/10.1109/SIITME.2011.6102699>.  
45
- 46 [84] J.D. Wang, N.J. Douville, S. Takayama, M. ElSayed, Quantitative analysis of molecular  
47 absorption into PDMS microfluidic channels, *Ann Biomed Eng*, 40(2012) 1862-1873.  
48
- 49 [85] M. Mastrangeli, S. Millet, T. Orchid Partners, J. Van den Eijnden-van Raaij, Organ-on-  
50  
51  
52  
53  
54  
55  
56  
57  
58  
59  
60

- 1  
2  
3  
4  
5  
6  
7 chip in development: Towards a roadmap for organs-on-chip, *ALTEX-Altern Anim Exp*,  
8 36(2019) 650-668.  
9
- [86] A. Sontheimer-Phelps, B.A. Hassell, D.E. Ingber, Modelling cancer in microfluidic  
10 human organs-on-chips, *Nat Rev Cancer*, 19(2019) 65-81.  
11
- [87] B.J. van Meer, H. de Vries, K.S.A. Firth, J. van Weerd, L.G.J. Tertoolen, H.B.J. Karperien,  
12 P. Jonkheijm, C.Denning, A.P. IJzerman, C.L. Mummery, Small molecule absorption by  
13 PDMS in the context of drug response bioassays, *Biochem Biophys Res Commun*,  
14 482(2017) 323-328.  
15  
16  
17  
18  
19
- [88] R. Prantil-Baun, R. Novak, D. Das, M.R. Somayaji, A. Przekwas, D.E. Ingber,  
20 Physiologically based pharmacokinetic and pharmacodynamic analysis enabled by  
21 microfluidically linked Organs-on-Chips, *Annu Rev Pharmacol Toxicol*, 58(2018) 37-64.  
22  
23  
24  
25
- [89] A.W. Auner, K.M. Tasneem, D.A. Markov, L.J. McCawley, M.S. Hutson, Chemical-  
26 PDMS binding kinetics and implications for bioavailability in microfluidic devices, *Lab*  
27 *Chip*, 19(2019) 864-874.  
28  
29  
30  
31  
32  
33  
34  
35  
36  
37  
38  
39  
40  
41  
42  
43  
44  
45  
46  
47  
48  
49  
50  
51  
52  
53  
54  
55  
56  
57  
58  
59  
60



## Figure Captions

**Fig. 1:** Design of the multi-organ-on-a-chip with a MEA, by assuming the measurement of electrophysiological activities of cardiac tissues. (a) Schematic zoomed-in view of the device, showing a structure with three PDMS layers bonded to a glass substrate, from top to bottom: a perfusion layer, an MEA layer, and a control layer. (b) Schematic of the side view of the device. The parylene-C insulating layer for the MEA is indicated in green. The inset shows a microvalve in normally open “push-up” configuration. (c) Photomask design of three-layers structure and its realistic top view. The microchannels and two cell culture chambers and the sample inlet/outlet holes in the perfusion layer are indicated in blue, whereas the control channel and the pressure inlet hole in the control layer is indicated in green. The peristaltic micropump consisting of three chambers arranged at 500  $\mu\text{m}$  intervals is located between two cell-culture chambers. The MEA and the reference electrode are indicated in orange. 1) Heart cell chamber, 2) Liver cell chamber, 3) MEA, and 4) Micropump. (d) Image of the device and close-up views of the heart cell chamber and microvalve. The rounded profile makes the (air-filled) flow channel appear darker than the control channel with a rectangular cross-section in the brightfield micrograph.

**Fig. 2:** Electrode layout and relevant dimensions of the MEA.

**Fig. 3:** Finite element analysis of the  $200 \times 200 \mu\text{m}^2$  square PDMS membrane deformation. (a) Simulated cross-sectional profile of the deformed PDMS membrane having a thickness of 20  $\mu\text{m}$ ; the applied pressure ranges from 5 to 65 kPa with a step of 15 kPa. (b) Design of the microvalve formed by the flow channel crossing control channel and 3D profile of the PDMS membrane deformed at a pressure of 57 kPa to seal the follow channel with a height of 45  $\mu\text{m}$ , considering a contact analysis of the PDMS membrane deformation in the flow channel. The red line on the flow channel represents the simulated profile under a pressure of 65 kPa, in Fig. 3a. (c) Simulated 3D profiles of deformed PDMS membrane contacting the flow channel.

**Fig. 4:** Schematic of the microfabrication of the device. (a) Fabrication process of the device. Perfusion layer: (p-1) Standard lithography for the cell culture chambers. (p-2) UV exposure with DMD-based grayscale lithography for the fluidic channel. (p-3) Development. (p-4)

1  
2  
3  
4  
5  
6  
7 PDMS casting and cutting partially at the cut line to accommodate the contact pads of MEA.  
8 MEA layer: (m-1) Patterning Au electrodes and sandwiching parylene-C layer. (m-2) Spin-  
9 coating the PDMS film. Control layer: (c-1) Standard lithography for the control channel. (c-2)  
10 PDMS casting. After the MEA and control layer fabrication: (m/c-1) Bonding two layers with  
11 uncured PDMS adhesive and peeling off from the Si substrate. (m/c-2) O<sub>2</sub> plasma etching for  
12 opening the electrode site and parylene-C removal except for the MEA components. Finally,  
13 this structure is bonded to the perfusion layer, followed by the glass substrate, using uncured  
14 PDMS adhesive (in p/m/c/glass). (b) Cross-section view of the MEA layer fabrication process  
15 in detail. (m-1a) Parylene-C deposition. (m-1b) Positive photoresist patterning. (m-1c) O<sub>2</sub>  
16 plasma etching for the electrode sites. (m-1d) Au deposition. (m-1e) Patterning the Au film for  
17 MEA. (m-1f) Parylene-C deposition. (c) Cross-section view of the bonded MEA and detailed  
18 control layer fabrication process. (m/c-2a) Removal of Si carrier substrate. (m/c-2b) O<sub>2</sub> plasma  
19 etching for opening the electrode site. (m/c-2c) O<sub>2</sub> plasma etching of parylene-C in the small  
20 gap formed by the bulk-PDMS mask. (m/c-2d) Mechanical removal of parylene-C for the MEA  
21 components.  
22  
23  
24  
25  
26  
27  
28  
29  
30  
31  
32  
33

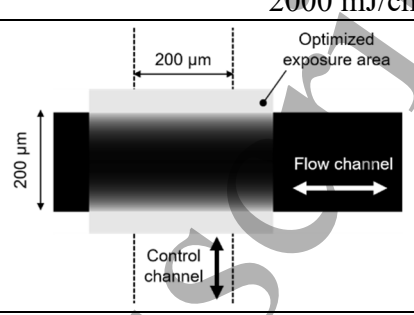
34 **Fig. 5:** Schematic illustration for sequence of the micropump actuation units from top view  
35 and actuation time intervals for each solenoid valve.  
36  
37

38  
39 **Fig. 6:** Measured volumetric flow rates of the cell-culture medium in the device operated using  
40 the integrated micropump. (a) Pressure-dependent actuation at a frequency of 1.5 Hz. (b)  
41 Frequency-dependent actuation at an applied pressure of 150 kPa.  
42  
43  
44  
45

46 **Fig. 7:** Comparison between the stylus measurement and the target profile.  
47  
48

49 **Fig. 8:** Impedance magnitude (a) and phase (b) spectra of electrode sites with different  
50 diameters in a PBS solution. The inset shows the image of the fabricated parylene-C-  
51 sandwiched Au electrodes arranged in the form of a 3×6 array. The frontside of the electrodes  
52 is etched open under O<sub>2</sub> plasma.  
53  
54  
55  
56  
57  
58  
59  
60

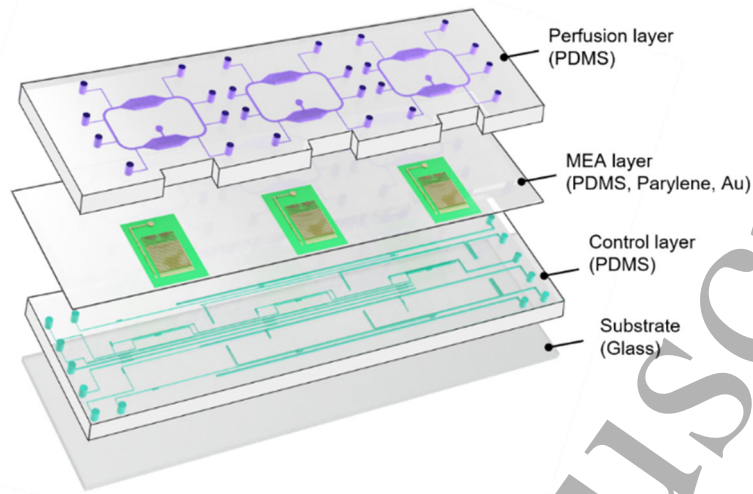
**Table I:** Summary of the process parameters optimized for the flow channel fabrication with DMD-based grayscale lithography.

Process	Parameter	
UV Exposure	Maximum dose	2000 mJ/cm <sup>2</sup>
	Digital mask data	
	Focal position	22.5 μm
Development (at 21 °C)	Time	550 s

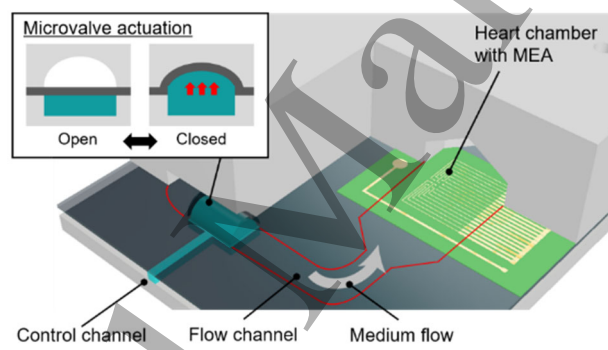
**Table II:** Measured impedance and phase values at 1 kHz of MEA electrodes.

Diameter [μm]	Impedance [kΩ]	Phase [°]
80	48.2 ± 6.44	-79.2 ± 2.32
90	36.9 ± 5.54	-80.2 ± 1.98
100	33.2 ± 6.03	-81.0 ± 0.84

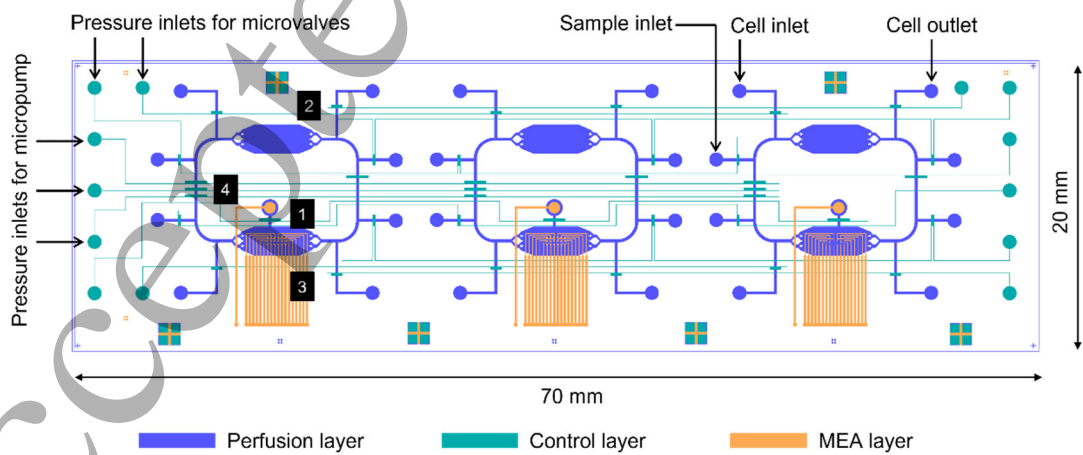
(a)



(b)



(c)



(d)

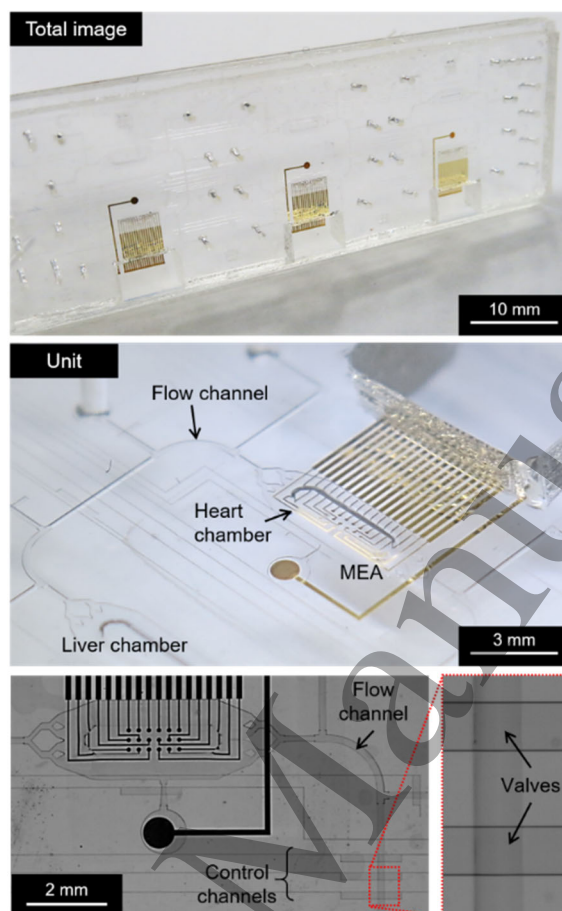


Fig. 1.

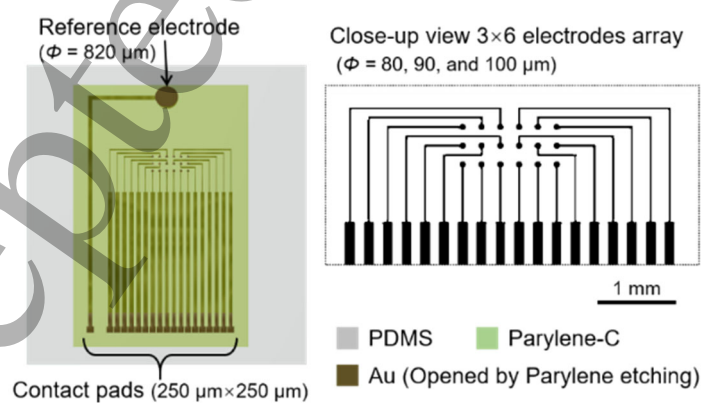
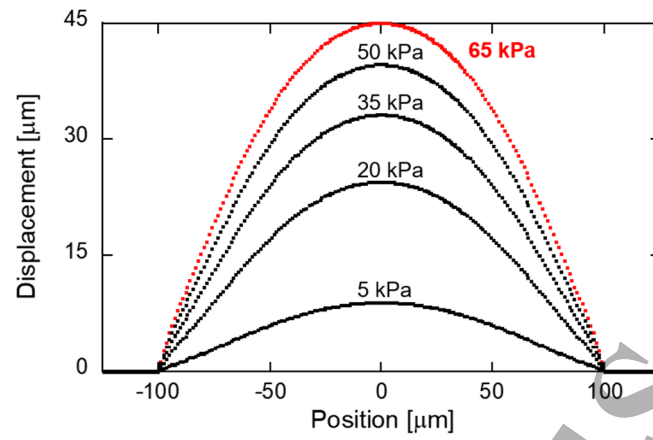
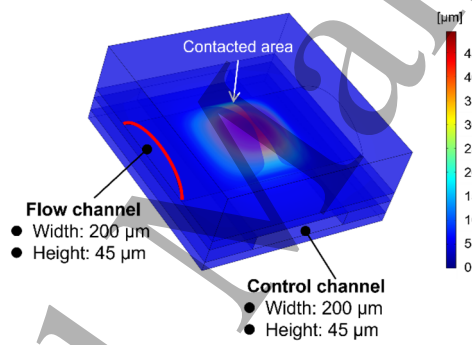


Fig. 2.

(a)



(b)



(c)

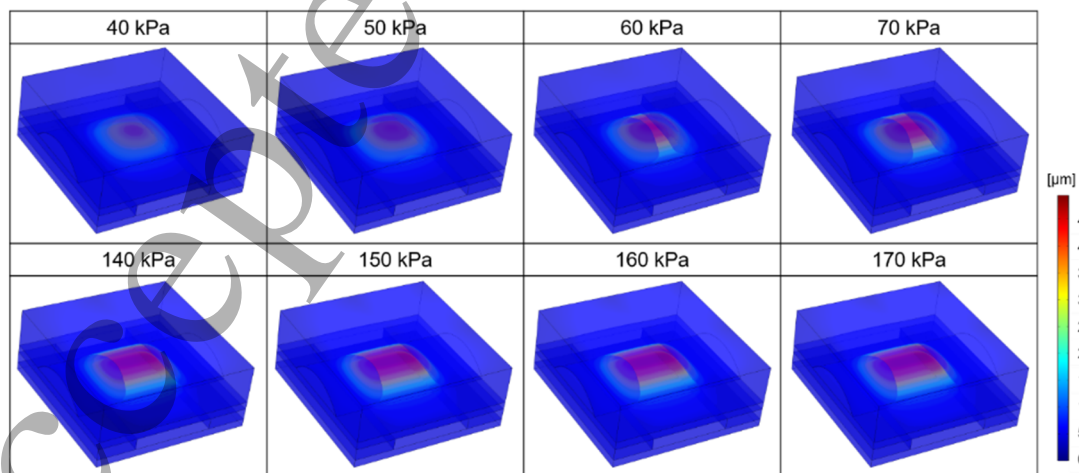


Fig. 3.

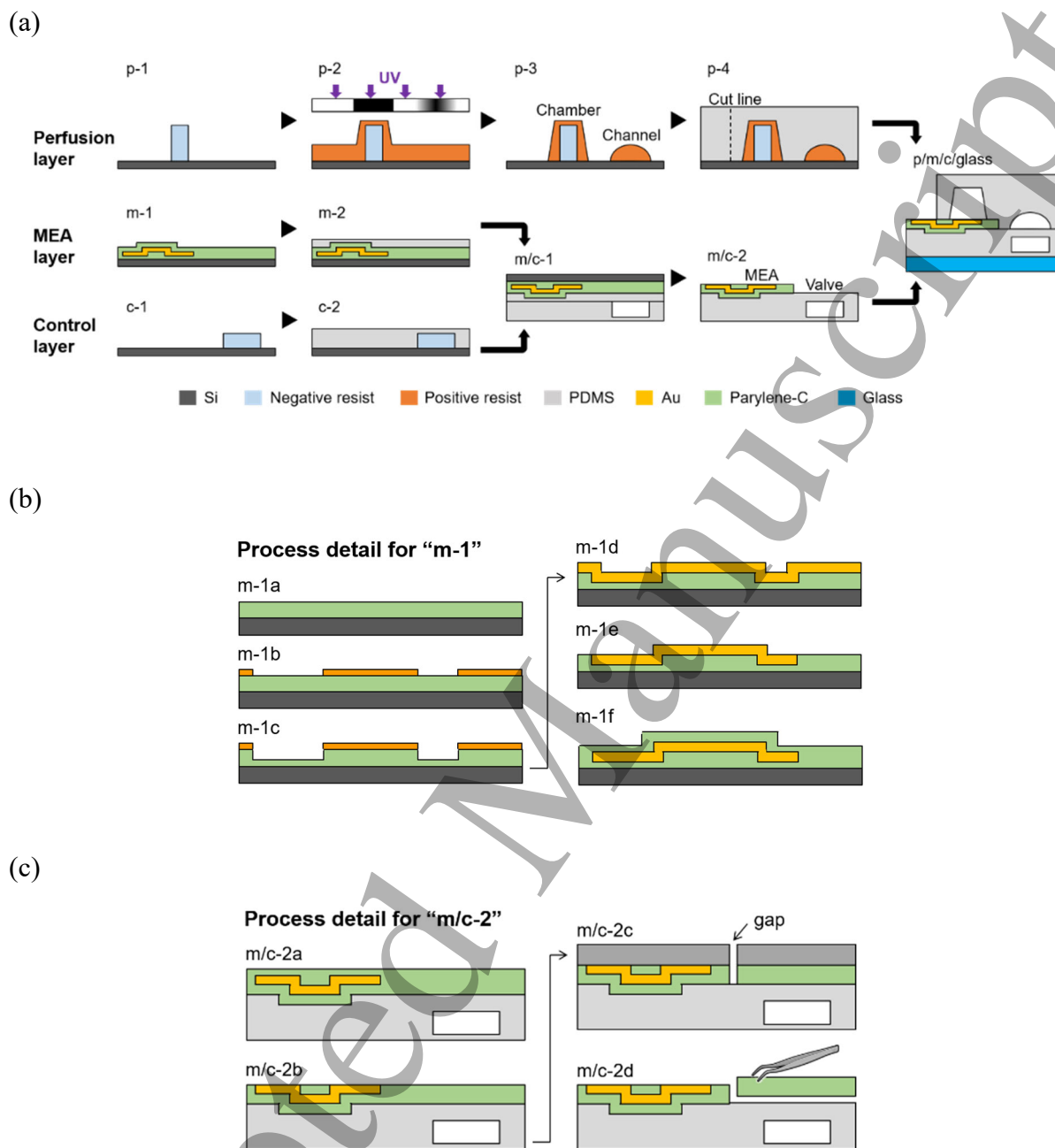


Fig. 4.

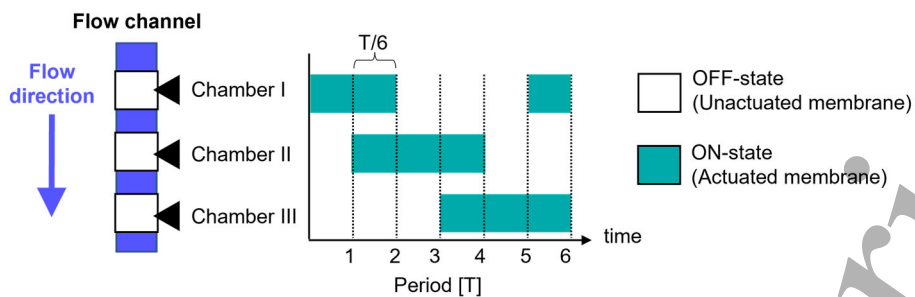
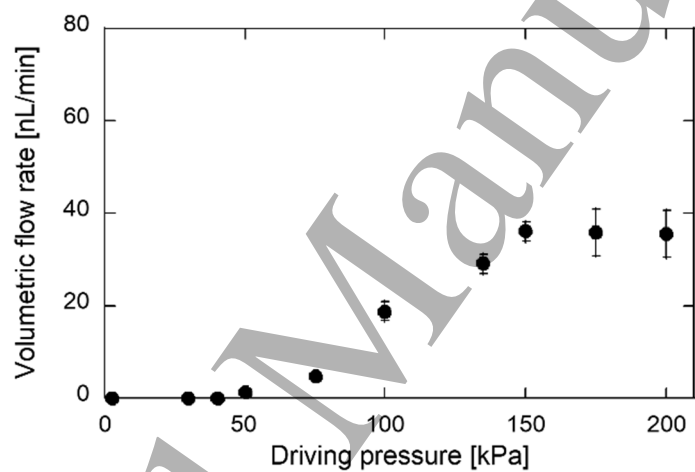


Fig. 5.

(a)



(b)

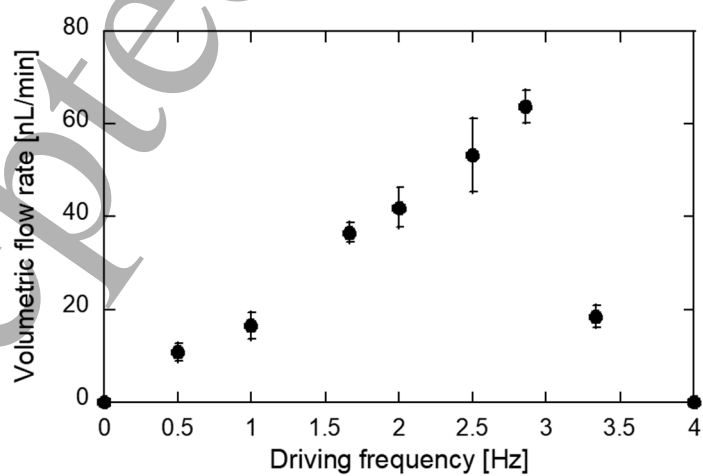


Fig. 6.



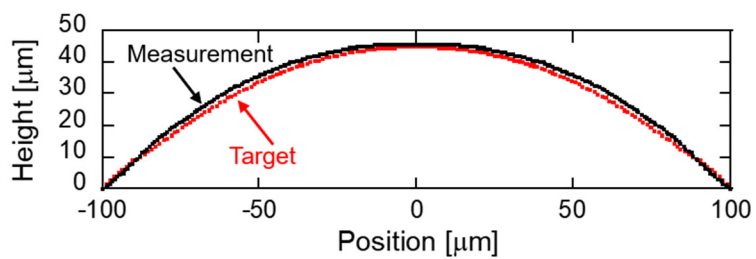
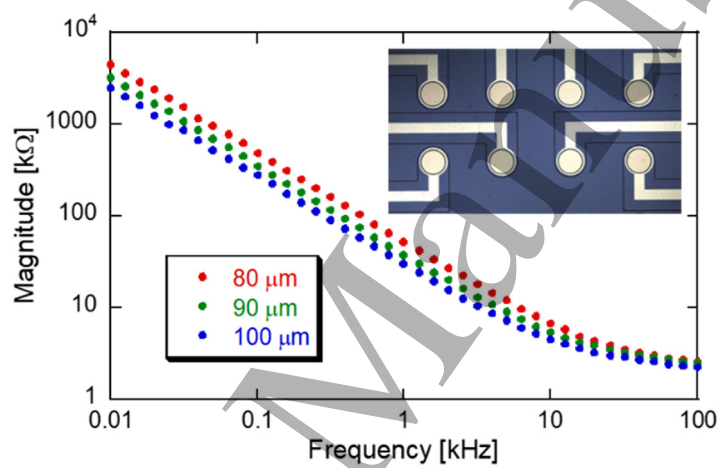


Fig. 7.

(a)



(b)

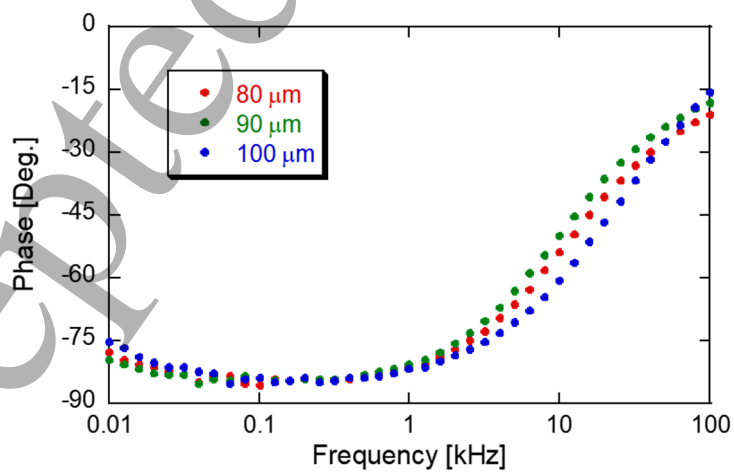


Fig. 8.